armor wires were inspected for kinks or other deformations; none were found. The conductors were uncabled. Each conductor's shielding tape was removed and inspected for cracks and knuckling; none were found. The insulation shields were examined for deformation or abrasion; there was no abrasion and only slight local deformation from shielding tapes due to load cycling. Insulation shielding was stripped from the insulation and actually showed improved bonding over untested core. This was probably due to the heat effect. There was no area to be found with lack of adhesion, confirming what the partial discharge test had indicated. Insulation was examined for signs of treeing, cavities, voids, and separations; none were found. The bond between the insulation and extruded conductor shield was examined, and no signs of separation were found. The copper strands comprising the conductor were perfectly formed with no evidence of kinks.

Finally, the two temporary splices were dissected and inspected. The semiconducting insulation shielding tapes were found to be not completely in contact with the insulation. Cavities were revealed between the EPR insulation and the shielding tapes, and a residue was found on the insulation surface where ionization had occurred. No electrical trees were found. These findings were the result of temporary splice procedures. The presence of these cavities served—however unintentionally—to show that EPR insulation can withstand long periods of ionization without voltage breakdown.

Just prior to removing the cable test specimen from the apparatus, photographs of the cable bends were taken to permit bend radii to be determined. From these photos, it was found that the cable had been bent as tightly as a 3.29-ft radius, exceeding the 4-ft minimum recommended cable bend radius.

VII. CONCLUSIONS

It would, of course, be valuable to repeat this test and to extend the parameters. The apparatus could be modified for increased or variable angles of flexing, with perhaps the addition of torsional moments. This test program was terminated after seven weeks to provide the results of physical examination to our customer prior to the solicitation of the first full scale system. At face value, the equivalent operating life of 36.7 years is in excess of expected system life. However, it must be taken into account that we are extrapolating from one test on a single short sample, a sample which, in fact, had not yet failed and did not show evidence of incipient failure. This makes it difficult to project a reliable expected service life on the order of the 30-year life desired. Additional testing using the equipment herein described or with possible refinements is a matter for economic consideration.

Passive Systems Theory with Narrow-Band and Linear Constraints: Part II—Temporal Diversity

JOSE M. F. MOURA

Abstract—This paper is part of a series of three papers studying passive tracking problems arising in navigation and positioning applications. The basic question here lies with the determination of the position and dynamics of a point source being tracked by an omnidirectional observer, through demodulation of the Doppler effect induced on the radiated signals by the relative motions. A simple model, fitting a finite parameter nonlinear estimation context, is developed, the receiver designed, and its mean-square error performance studied. It is shown that, besides the speed and angle estimation, simultaneous global range passive tracking is possible. The signal model precludes range acquisition from synchronous measurement of the absolute phase reference: the global range estimation is attained by processing the higher order temporal modulations (varying Doppler). Quantifying the statistical and geometric performance tradeoffs, the work presents simple expressions and graphical displays that can be used as design tools in practical passive tracking problems. A subsequent paper considers the space/time coupling issues, generalizing the study to the context where a moving source is tracked by a directional array.

I. INTRODUCTION

EVERYBODY has experienced the Doppler phenomenon. The whistling of an approaching train is heard at a higher note than the whistling of an outgoing train. This frequency shift is the Doppler effect, important in a number of applications. Doppler radars [1] estimate from it the radial speed of moving platforms. In synthetic aperture radars (SAR) [2], it focuses the radiated beam on the azimuth dimension. In radio astronomy [3], it resolves radio sources. In super synthetic techniques [4], advantage is taken of the earth motion itself to generate very long baseline (VLB) arrays.

Hagfors and Campbell [5] discuss a VLB interferometer that probes the Moon or Venus surface by processing the unequal Doppler shifts caused by the different speeds of the planet's valleys and mountains, as seen along the line of sight of the earth radar. Doppler related examples are still found in many other fields, e.g., oceanography [6], meteorology [7], and light diffusion interferometry [8].

This paper, together with Parts I [9] and III [10], studies passive practical procedures based on the Doppler phenomenon. Contrasting with active systems, passive ones (e.g., passive sonars) process signals radiated by sources other than the receiver. To be brief, the passive Doppler problems are herein cataloged into two dual classes (see Fig. 1): 1) positioning if the source is to be tracked, and 2) navigation if the source, of known position and dynamics, is a navigational aid (e.g., a beacon or·a satellite). The subsequent discussion concentrates on the positioning context.

In the framework of communication theory, the Doppler phenomenon is a modulation induced on the signal's phase structure by an extended source or receiver. This source or receiver extension, referred to as geometry diversity, may be the baseline of the observing array (spatial diversity), Fig. 1(a), or it may be synthetically developed by the relative motions (temporal diversity), Fig. 1(b). In the first case, the Doppler provides information to determine the bearing angle of the source. In the second case, it is a replica of the source-receiver's relative radial speed.

In both applications the Doppler is assumed to be a linear modulation; i.e., the observed frequency shift is considered constant during the observation interval. This constant Doppler corresponds to the source moving radially with respect to the receiver (see the configuration I of Fig. 2). This hypothesis, which underlies the design of radar systems [11], is justified on the grounds of a short observation interval. In general, the Doppler is a nonlinear modulation, as shown by geometry II of the same figure.

The present set of papers considers the design of processors (and the evaluation of their performance) that infer, from the modulated received waveforms, the relative geometry; i.e., it studies the simultaneous estimation of the source/receiver separation and dynamics. The basic novelty here is the determination of the global distance separating the source and the receiver from the observed Doppler.

In Part I [9], a fixed source is positioned by an extended observer, either spanned spatially by an array of sensors or generated synthetically by a moving sensor. This problem reduces to the estimation of two parameters, range and bearing, from narrow-band passive signals. Part II (this paper) enlarges the class of passive tracking problems to include nonstationary sources. At this stage, to avoid masking the fundamental issue of global identifiability with unnecessary complexity, the study is restricted to: 1) deterministic and linear source dynamics, 2) omnidirectional receivers, and 3) narrow-band radiated signals. The ensuing framework is that of a three-parameter nonlinear estimation problem. Part III [10] foregoes the simplifying assumption 2) and studies the general problem of tracking moving sources observed by spatially extended receivers. Spatial and temporal coupling issues are discussed
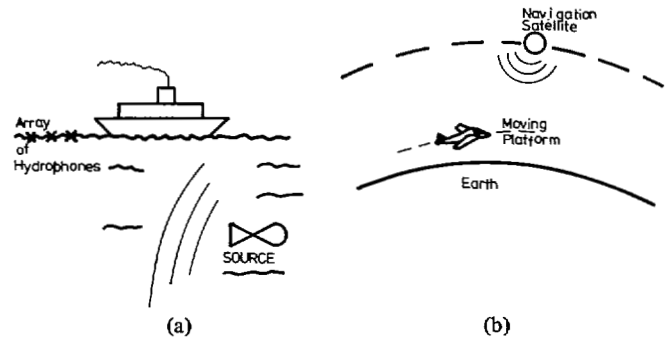

Fig. 1. Positioning and navigation applications. (a) Positioning (spatial diversity). (b) Navigation (temporal diversity).
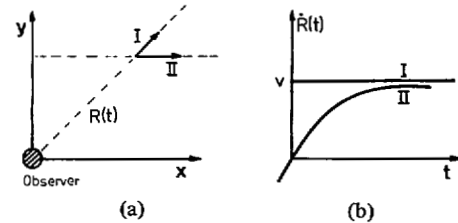

Fig. 2. Temporal Doppler variation for two geometries. (a) Source/observer geometry. (b) Doppler.

therein. The absence of hypotheses 1) and 3) is considered in [12].

The structure of the paper is as follows. Section II establishes the model, discussing the constraints imposed on the problem. Section III designs the receiver. Sections IV and V analyze the receiver structure, while Section VI studies its performance and presents Monte Carlo simulation results.

II. MODEL

The basic model constraints relate to the geometric aspects of the problem, to the relative dynamics, and to the nature of the radiated signals and disturbing noises. Fig. 3 illustrates a typical positioning application where an observer tracks a moving source by processing its radiated signature. The following assumptions are made.

Hypothesis 1: A Planar Geometry and a Stationary (Fixed) Omnidirectional Array: The array, with geometric dimension L, is centered at the origin of the reference frame (see Fig. 3).

Hypothesis 2: The Source Moves with a Constant Unknown Speed v Along a Linear Path: The instantaneous value of the source/receiver separation is parameterized as

$$R(t, l, A) = \{R_0{}^2 + v^2 t^2 - 2vt R_0 \sin \theta\}^{1/2},$$

$$t \in \left[-\frac{T}{2}, \frac{T}{2} \right]. \tag{1}$$

In (1), t is the time, and l is the location of the array sensors. Equation (1) defines $R(t, l, A)$ in terms of the parameters: the range R_0, the speed v, and the angle θ all given in Fig. 3. These parameters are collected in the unknown nonrandom parameter vector

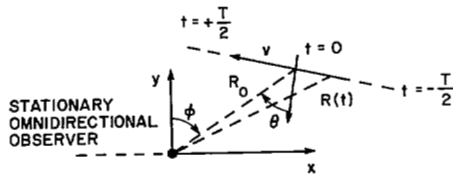$$A = [R_0 v \sin \theta]^T \tag{2}$$

Fig. 3. Stationary array/moving source.

where T denotes matrix transposition.

For a different class of motions, some functional form other than (1) would result. But, provided the hypothesis on the deterministic dynamics is kept, the separation can be fitted by a finitely parameterized function.

Hypothesis 3: The Source Signature $s(t, l)$ is Narrow Band: A Pure Tone of Known Rest Frequency $f = \omega_c/2\pi$: At the array, a corrupted delayed version $r(t, l)$ of $s(t, l)$ is received. The propagation delay $\tau(t, l, A)$ is approximately given by

$$\tau(t, l, A) \cong \frac{R(t, l, A)}{c} \tag{3}$$

where c is the waveform propagation speed in the medium.[1] The parameter vector A is nonlinearly modulated on the signal structure by this delay.

Recalling the complex notation of Part I [9], the received signal is

$$r(t, l) = \sqrt{2}\ \text{Re}\ \{\tilde{r}(t, l) \exp j\omega_c t\} \tag{4}$$

where the complex amplitude

$$\tilde{r}(t, l) = \tilde{s}(t, l, A) + \tilde{w}(t, l). \tag{5}$$

$\tilde{w}(t, l)$ is a zero mean, spatially and temporally "white" Gaussian noise with double spectral height of N_0. The signal complex envelope is

$$\tilde{s}(t, l, A) = \sqrt{E_r}\tilde{b}\tilde{s}_n(t, l, A) \tag{6}$$

with $\tilde{s}_n$ being a normalized signal

$$\tilde{s}_n(t, l, A) = \frac{1}{\sqrt{LT}} \exp\left[-j\frac{2\pi}{\lambda}R(t, l, A)\right],$$
$$t \in \left[-\frac{T}{2}, \frac{T}{2}\right], \qquad l \in \left[-\frac{L}{2}, \frac{L}{2}\right]. \tag{7}$$

In the preceding equations, as in Part I [9], $E_r = PLT =$ energy x length received during the observation interval $[-T/2, T/2]$, $P =$ signal power; $\lambda = c/f =$ wavelength; $\tilde{b} = b \exp j\psi$, with b Rayleigh and ψ uniformly distributed random variables. The zero mean Gaussian random variable $\tilde{b}$, with variance $2\sigma_b^2$, is independent of the measurement noise $\tilde{w}(t, l)$. It accounts for model inaccuracies and for radiated signal power variations

fading in the transmission medium. Of more significance, however, as pointed out in Part I [9], $\tilde{b}$ rules out knowledge of the signal absolute phase. The receiver is incoherent, precluding the estimation of the range through simple measurement of constant travel time delay, as in synchronized systems [13]. The problem rests then on the reconstruction of the range function (i.e., the three source parameters) solely from the temporal phase modulation induced by the relative dynamics.

By a Taylor's series expansion of (1)

$$R(t, l) \cong R_0 - (v \sin \theta)t - \frac{v^2 \cos^2 \theta}{R_0} \frac{t^2}{2!}$$
$$+ 3\frac{v^2 \cos^2 \theta}{R_0} \frac{v \sin \theta}{R_0} \frac{t^3}{3!} + \cdots . \tag{8}$$

Since the signal model assumes no knowledge of the absolute phase, the information about the source parameters relies upon the higher order terms of the Taylor series expansion of (1) as shown in (8). For small observation intervals, (8) can be truncated at the linear term: the observer measures the source down-range velocity component. This is equivalent to the usual far-field assumption in wave theory, see Part I [9], or to trajectory I of Fig. 2. It finds practical application in navigation, with radiolocation systems utilizing phase information to measure velocity, or when tracing remote platforms such as dropsondes, balloons for measuring wind, and drifting buoys for collecting oceanographic data. A receiver is installed on the moving platform and the radio navigation information retransmitted to the base station. This base station determines the platform velocity (down-range) from the recorded incremental motion [14].

By further enlarging the observation interval, the second- (radial acceleration) and third-order effects can be measured. Since the transformation of coordinates among the three time derivatives $\dot{R}_0, \ddot{R}_0, \dddot{R}_0$ of the range function and the source parameters has a nonzero Jacobian

$$\frac{\partial(\dot{R}_0, \ddot{R}_0, \dddot{R}_0)}{\partial(R_0, v, \sin \theta)} = \frac{6v^5}{R_0^4} \cos^2 \theta \sin \theta \tag{9}$$

except for broadside ($\theta = 0$), end-fire ($\theta = -\pi/2$), or stationary target/receiver ($v = 0$) configurations, one concludes that up to third-order effects are sufficient for local specification of the source position and dynamics (implicit function theorem). That the Jacobian is zero for specific geometries may serve as a warning about possible difficulties at these configurations.

Three final remarks about the model assumed. First, the angle ϕ of Fig. 3 is not measurable from the observed data. This results from the absence of bearing angle discrimination at the observing array. Part III [10] introduces a directional array, studying the coupling arising between the space and time aspects. Here, the angle ϕ is ignored. Second, as seen from (1) or from (8), there is a model indetermination on the sign of v or $\sin \theta$. Therefore, in the sequel, $\sin \theta > 0$. Third, the model assumes a fixed (stationary) omnidirectional array. The results still carry out for moving omnidirectional observers, e.g., following a linear deterministic path with constant speed.
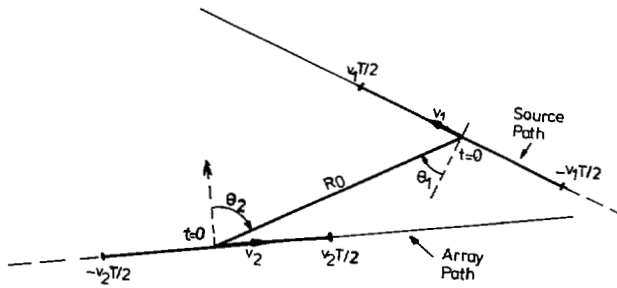
---

[1] In the sequel, the notation will often be simplified by suppressing from the list of the function's arguments some or all of t, l, and A.

Fig. 4.   Moving omnidirectional array/moving source.

The relative source parameters, besides R_0, are v and ϕ, defined by

$$v^2 = v_1{}^2 + v_2{}^2 + 2v_1 v_2 \cos (\phi_1 - \phi_2) \tag{10a}$$

$$\tan \phi = \frac{v_1 \sin \phi_1 + v_2 \sin \phi_2}{v_1 \cos \phi_1 + v_2 \cos \phi_2} \tag{10b}$$

where v_1, v_2, ϕ_1, and ϕ_2 are given in Fig. 4. For a parallel geometry

$$\left.\begin{array}{c} v_1 = v_2 \\ \phi_1 = \phi_2 \end{array}\right\} \Rightarrow \left\{\begin{array}{l} v = 2v_1 \\ \phi = \phi_1 = \phi_2. \end{array}\right. \tag{11}$$

In conclusion, the source/receiver dynamics generate a temporal baseline modulating the signal phase structure. The section cast the passive tracking problem in the framework of a finite parameter nonlinear estimation problem. Comparing with the spatial diversity problem of Part I [9], the temporal diversity model exhibits an additional parameter, namely the relative source speed v. Using a positioning terminology, this passive tracking application is referred to as a stationary array/moving source with omnidirectional sensor (SAMS$_o$) problem.

III. RECEIVER STRUCTURE

Applying maximum-likelihood (ML) techniques [11] to the estimation problem of Section II, the receiver is a matched filter followed by an envelope detector. It maximizes, see Part I [9], the log ML function defined by

$$\ln \Lambda_1(A) = \frac{1}{N_0} \frac{\bar{E}_r/N_0}{1 + \bar{E}_r/N_0} \mid \tilde{L}(\bar{A}) \mid^2 \tag{12}$$

where $\bar{E}_r$ = average received energy = $2\sigma_b{}^2 E_r$ and $L(\bar{A})$ is the inner product

$$\mid \tilde{L}(\bar{A}) \mid^2 = \left| \int_{-T/2}^{T/2} dt \int_{-L/2}^{L/2} dl \, \tilde{r}(t, l)\tilde{s}^*(t, l, \bar{A}) \right|^2 \tag{13}$$

between the received waveform $\tilde{r}$ and a replica of the signal $\tilde{s}$ evaluated at the scanning point $\bar{A}$ in the A-parameter space Ω. Substituting the value of the received signal by (5) in (13)

$$\mid \tilde{L}(\bar{A}) \mid^2 = \mid \langle \tilde{s}(A), \tilde{s}(\bar{A}) \rangle + \langle \tilde{w}, \tilde{s}(\bar{A}) \rangle \mid^2. \tag{14}$$

In the absence of additive measurement noise, $\tilde{L}(A)$ is a scaled
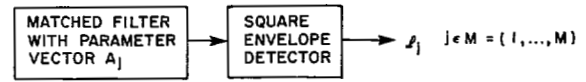

Fig. 5.   Coarse search ML algorithm.

version of the signal autocorrelation function

$$\Psi(A, \bar{A}) \triangleq \langle \tilde{s}_n(A), \tilde{s}_n(\bar{A}) \rangle \tag{15}$$

where $\tilde{s}_n(A)$ is the normalized signal (7), evaluated at the actual parameter value A. The output of the ML receiver is, apart from a multiplicative gain, the squared modulus of the autocorrelation function

$$\Phi(A, \bar{A}) = \mid \Psi(A, \bar{A}) \mid^2. \tag{16}$$

In analogy with active radar and sonar theory, function $\Phi(A, \bar{A})$ is referred to as the generalized ambiguity function (GAF).

The second term in (14) represents a Gaussian complex random variable with zero mean and variance N_0. At two different scanning points of the parameter space Ω, the noise samples at the output of the matched filter exhibit a cross correlation given in terms of $\Psi(A, \bar{A})$.

Since this function has essentially a finite extent, as shown below, a coherence or correlation distance can be defined in Ω: scanning points whose separation is greater than the coherence distance lead to uncorrelated noise components at the output of the ML processor. This justifies a two-step implementation of the ML algorithm, first due to Woodward [15], known in the frequency estimation literature as frequency shift keying (FSK).

The first step substitutes the continuous by a discretized search where the scanned points are separated by the coherence distance. Ω is divided into M cells, the form of which is to be found; in each cell it is assumed that the parameter vector A takes only a fixed value (e.g., the center of the cell). With Ω so discretized, a crude maximization of the log ML function is performed, computing it at all grid vertices, and choosing the point at which it is maximum. The receiver performs a "largest of" M-ary hypothesis decision [16] with uncorrelated signals; at this stage it has a three-dimensional bank of matched filters followed by square envelope detectors (see Fig. 5).

The coarse search returns a crude estimate $\tilde{A}_{ml} = A_i$ for which $l_i = \max l_j$ (see Fig. 5). In the second step, the mechanism accomplishes a local maximization of the log ML function about $\tilde{A}_{ml}$.

It remains to ascertain the following points: 1) the finite extent of the signal autocorrelation function or, to that effect, of the generalized ambiguity function, 2) the form and dimensions of the grid cells in the ML algorithm, and 3) the statistical behavior and bounds on the mean-square error performance of the ML receiver. The subsequent sections treat separately each one of these topics.

IV. GENERALIZED AMBIGUITY FUNCTION

As discussed previously, the receiver's ability to locate the source is connected to the GAF structure. Due to the analytical complexity of the GAF's expression (16), its structure is
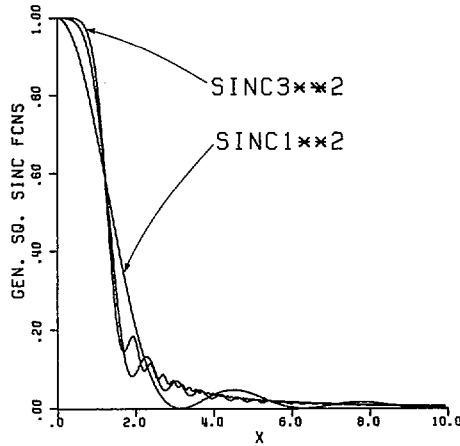
Fig. 6.   Generalized $\text{sinc}_n{}^2$ functions up to third-order.

studied graphically. First, however, an approximate study is carried out, assuming the third-order expansion (8) to the range function. It serves to derive simple expressions that easily illustrate the basic GAF structure.

A. Polynominal Approximation to the Range Function

Since the source parameters may be recovered from the Doppler $\dot{R}_0$, the radial acceleration $\ddot{R}_0$, and the third-order time derivative $\dddot{R}_0$, the argument proceeds in terms of these coefficients.

In the sequel, the following definition is needed.

Definition: the $\text{sinc}_n{}^2$ function of nth order is given by

$$\text{sinc}_n{}^2 \ (\Sigma) = \left| \frac{1}{2\Sigma} \int_{-\Sigma}^{\Sigma} \exp j\tau^n \ d\tau \right|^2 . \tag{17}$$

Taking as origin the actual source location along the $\dot{R}_0$, $\ddot{R}_0$, and $\dddot{R}_0$ axes, the ambiguity function is given, respectively, by

$$\text{sinc}_1{}^2 \ (\Sigma) = \text{sinc}^2 \ (\Sigma) = (\sin \Sigma/\Sigma)^2 \tag{18a}$$

$\text{sinc}_2{}^2 \ (\Sigma)$ (related to Fresnel integrals), and

$$\text{sinc}_3{}^2 = \left| \frac{1}{\Sigma} \int_0^{\Sigma} \cos \tau^3 \ d\tau \right|^2 . \tag{18b}$$

Notice that

$$\lim_{\Sigma \to \infty} \int_0^{\Sigma} \cos \tau^3 \ d\tau = \frac{\pi \text{Ai}(0)}{3^{1/3}} = \frac{\pi}{3\Gamma\left(\dfrac{2}{3}\right)} \approx 0.765 \tag{18c}$$

where Ai (0) is the Airy function [17]. In the preceding expressions Σ is a measure of the deviation along the axes.

Fig. 6 compares these $\text{sinc}_n{}^2$ functions. All exhibit a main lobe and secondary ripples. As the order n increases, the main lobe is flatter near the origin, while the ripples die out faster. The rate of falloff is found by studying the asymptotic behavior as done in (18c). All three functions are bounded by $1/\Sigma^2$.

(a)

(b)
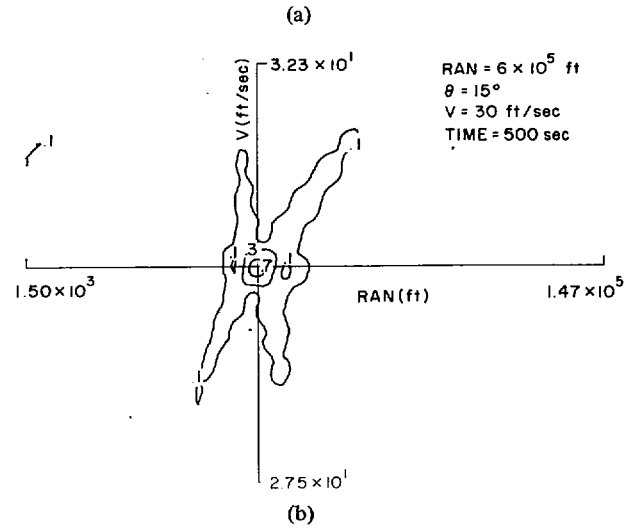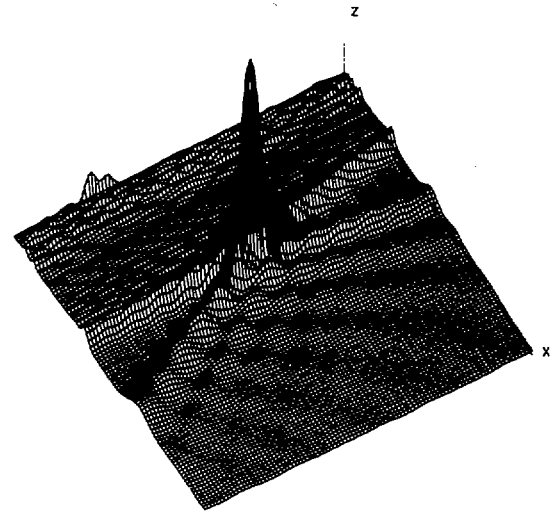
Fig. 7.   (a) Three-dimensional range/velocity ambiguity structure ($X = 1/8$). (b) Contour range/velocity ambiguity structure ($X = 1/8$).

Outside the axes, as the scanning point departs from the origin, the GAF's behavior can be approximated by an Airy function (see [12]) being bounded by the inverse of a certain power of the mismatch on the parameters. This asymptotic behavior is referred to here as the GAF *hyperbolic secondary structure*.

B. General Case

The generalized ambiguity function, given by (16), is studied graphically for the SAMS$_0$ context. The source actual parameters are assumed fixed:

$$A_a = \begin{bmatrix} R_{0_a} \\ v_a \\ \sin \theta_a \end{bmatrix} = \begin{bmatrix} 0.6 \times 10^5 \text{ ft} \\ 30 \text{ ft/s} \\ \sin 15^\circ \end{bmatrix} . \tag{19}$$

Figs. 7 and 8 show three-dimensional and contour plots of the GAF on the coordinate planes (see also Fig. 6 in Part I [9]). The figures illustrate intuitively the behavior of the ML processor as that of a peaking circuit. Looking at them, one ventures that, at least for a low noise profile, the ML estimate is

(a)

RAN = 6×10^5 ft
$\theta = 15°$
V = 30 ft/sec
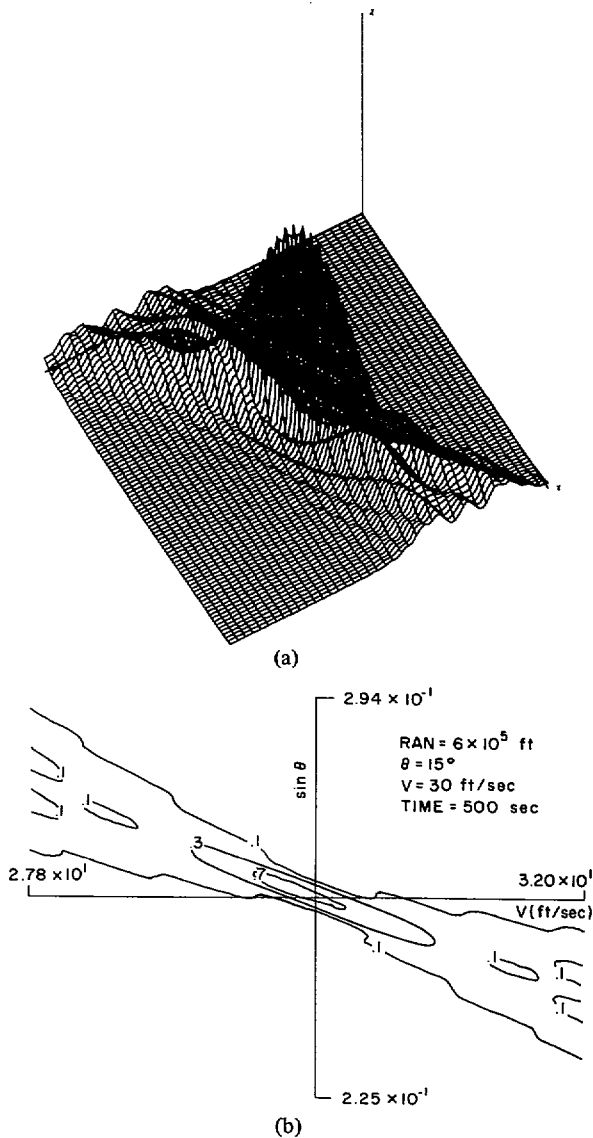TIME = 500 sec

(b)

Fig. 8.   (a) Three-dimensional velocity/angle ambiguity structure ($X = 1/8$).   (b) Contour velocity/angle ambiguity structure ($X = 1/8$).

near the actual source location; how near will be quantified by the error analysis of Section VI. Note in Fig. 8 the shearing of GAF, much like what happens in Chirp (linear frequency modulated) continuous active waveform radars (see [11]). For these figures, the modulating index defined by the geometric parameter

$$X = vT/2R_0 \qquad (20)$$

is 1/8. Plots for other values of X are in [12].

These graphs confirm the approximate analysis conclusions of the previous paragraph: 1) the GAF presents a main lobe centered at the source position at $t = 0$ (midpoint of the observation interval), and 2) negligible subsidiary peaks ignored in the subsequent error analysis.

The contour plots exhibit the main lobe equal height contours as approximate ellipses, suggesting that the three-dimensional ones are roughly ellipsoids. This is confirmed by looking at the equal height contours of the GAF main lobe on planes
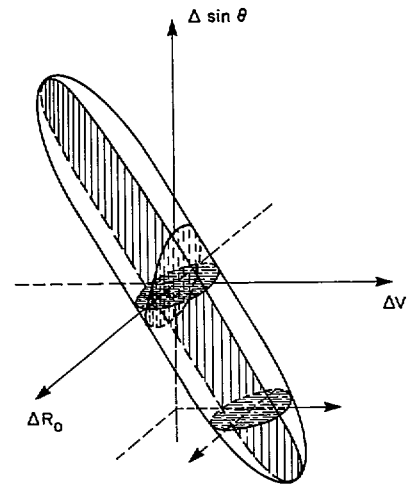

Fig. 9.   Main lobe ellipsoidal structure.

parallel to the coordinate axes planes. Fig. 9 shows one of these ellipsoids. The configuration is referred to as the main lobe ellipsoidal structure. It plays an important role in performance studies, since it determines the form and dimension of the elementary cells of the ML grid.

The rate of falloff of the GAF secondary structure is studied in [12] by resorting to the method of stationary phase, e.g., [18]. The study therein substantiates the *hyperbolic decaying* conclusion of the approximate analysis.

In short, both the approximate and the graphical studies show that GAF is peaked, exhibiting: 1) a main lobe ellipsoidal structure, and 2) a hyperbolic secondary negligible structure with the GAF decaying with the inverse of a certain power of the parameter errors on Ω.

The GAF's peaked structure establishes the model global identifiability; it is possible to estimate globally and simultaneously all of the source parameters from the sensor measurements.

V. QUADRATIC EXPANSION OF THE GENERALIZED AMBIGUITY FUNCTION

The foregoing analysis indicates that on the parameter space Ω the significant GAF is restricted to a vicinity of the actual source location. As in Part I [9], the ambiguity function is then approximated by the quadratic expansion

$$\Phi(A, A_a) \cong 1 - \Delta A^T M \Delta A \qquad (21a)$$

where $\Delta A = A - A_a$ and

$$M = -\frac{1}{2}\left[\frac{\partial^2 \Phi(A, A_a)}{\partial A_i A_j}\bigg|_{A=A_a}\right]_{i,j} \qquad (21b)$$

is the mean-square spread matrix. The finite extent of GAF is measured by the ellipsoid

$$Q(\Delta A) \triangleq \Delta A^T M \Delta A \cong 1. \qquad (21c)$$

The spread matrix M is evaluated analytically in [12]. Given, however, its unappealing complexity, local, asymptotic, and

graphical analyses are pursued. Since the concern rests on the inverse M^{-1}, cross correlations, and det M which give on Ω the orientation, dimensions, and volume of the main lobe ellipsoid (and so of the grid cells of the ML estimation algorithm), attention is restricted to these quantities.

Assuming a short observation interval (local analysis), i.e., that $X = vT/2R_0 < 1$, Taylor's series expansions[2] lead to

$$M^{-1} = \left(\frac{\lambda}{2\pi}\right)^2 \frac{5^2 \times 7}{X^6} \begin{bmatrix} \dfrac{1}{\sin^2\theta\cos^4\theta} & \dfrac{v}{R_0}\dfrac{1}{2\sin^2\theta\cos^2\theta} & -\dfrac{1}{R_0}\dfrac{1}{2\sin\theta\cos^2\theta} \\ = & \dfrac{v^2}{R_0^2}\dfrac{1}{4\sin^2\theta} & -\dfrac{v}{R_0^2}\dfrac{1}{4\sin\theta} \\ = & = & \dfrac{1}{R_0^2}\dfrac{1}{4} \end{bmatrix} \cdot \tag{22}$$

Fig. 10 shows, as a function of the geometric parameter X or its inverse $Y = 1/X$, the three diagonal elements of M^{-1}, normalized by the modulation index $\beta = \lambda/2\pi$. The source parameters are given in (19). Each graph displays the local $(X < 1)$ and asymptotic $(X \gg 1)$ tangents, as well as the corresponding analytical expressions. The convex cup behavior of $M_{R_0}^{-1}$ and $M_{\sin\theta}^{-1}$ in Fig. 10(a) and (b) is due to the phenomena analyzed in Part I [9]: for small X, the lobe is well spread over Ω with consequent small second-order derivatives of the GAF at the source location; for large X, the main lobe approaches a rectangular type window in the range/bearing subspace. For each geometry, then, there is an optimum observation time (i.e., an optimum value of X) above which the joint estimation of R_0 and $\sin\theta$ is 'deteriorated. In most applications, however, this geometry saturation occurs for unrealistically large values of X.

In Fig. 10(c) the inverse velocity spread M_v^{-1} is monotonically decreasing, evolving from the local to the asymptotic tangents. This behavior can be anticipated from Fig. 11: as the observation interval increases, the source goes from abeam (stationary Doppler) to down-range (Doppler approaching its maximum, the speed v).

Fig. 12 shows, also as a function of X, the cross correlations

$$\rho_{ij} = \frac{(M^{-1})_{ij}}{[(M^{-1})_{ii}(M^{-1})_{jj}]^{1/2}} \tag{23}$$

between the errors on the estimates for the several parameters. For small X the errors are highly correlated. As X increases, $\rho_{R_0,v}$ and $\rho_{v,\sin\theta}$ decrease monotonically, while $\rho_{R_0,\sin\theta}$ decreases first (reflecting reduction in correlation as higher order effects are measured) to increase again for large X

[2] The correct evaluation of these expressions requires that terms up to the 6th order be retained in the Taylor's series developments of the elements of the 3×3 matrix M. Part of the formidable manipulations involved in the inversion of the resulting analytic matrices were carried out with the use of MACSYMA, a symbol manipulating system, at Project MAC, Massachusetts Institute of Technology, Cambridge.

(rectangular type ambiguity function in the $\rho_{R_0/\sin\theta}$ subspace, see Part I [9]).

The determinant of M progresses from

$$\det M = \left(\frac{2\pi}{\lambda}\right)^6 \frac{R_0^4}{v^2} \frac{4\sin^2\theta\cos^4\theta X^{12}}{3^3 \times 5^3 \times 7} \tag{24}$$

for a short observation interval $(X < 1)$, to

$$\det M \sim \left(\frac{2\pi}{\lambda}\right)^6 \frac{R_0^4}{v^2} \frac{\pi}{2} \frac{1}{12} \frac{1}{\cos\theta} \frac{1}{Y} \tag{25}$$

for a long observation interval $(Y \ll 1)$.

The analytical expressions (22)–(25), as well as Figs. 10 and 12, may be used in each particular application, to dimension the grid cells of the ML algorithm, providing an easy check on the expected computational effort and on the error performance as will be seen in the next section. They were used in [12] as (pre-) design tools for radar and sonar passive processors in navigation and positioning problems.

Before proceeding, equivalent results are presented for situations when one of the three source parameters is assumed known a priori. This may be the case because either the parameter has been determined by some other means, or it represents a higher degree of complexity, or simply its incorporation in the estimation model makes no physical sense (e.g., source speed in the stationary source problem of Part I [9]). Since the range/angle estimation was studied in Part I [9], the analysis considers here the R_0/v and $v/\sin\theta$ joint estimation problem, being restricted to the short observation interval situation.

A. Range/Velocity Estimation – Application to Navigation

The bearing angle is assumed known. This might occur in some navigational applications, or when tracking satellites transmitting narrow-band signals. The latter is illustrated in Fig. 13. The array on Earth observes the satellite passing abeam. The duration of the observations is determined by the strength of the emitted signal and the receiving array gain. The observations are assumed symmetric about the raising angle (closest approach) determined, for example, from the position and the orientation of the stationary observer. In essence, the moving source follows a path that is prescribed or known a priori, the only unknowns being the source/receiver separation and the relative speed. The parameter vector is now $A =$
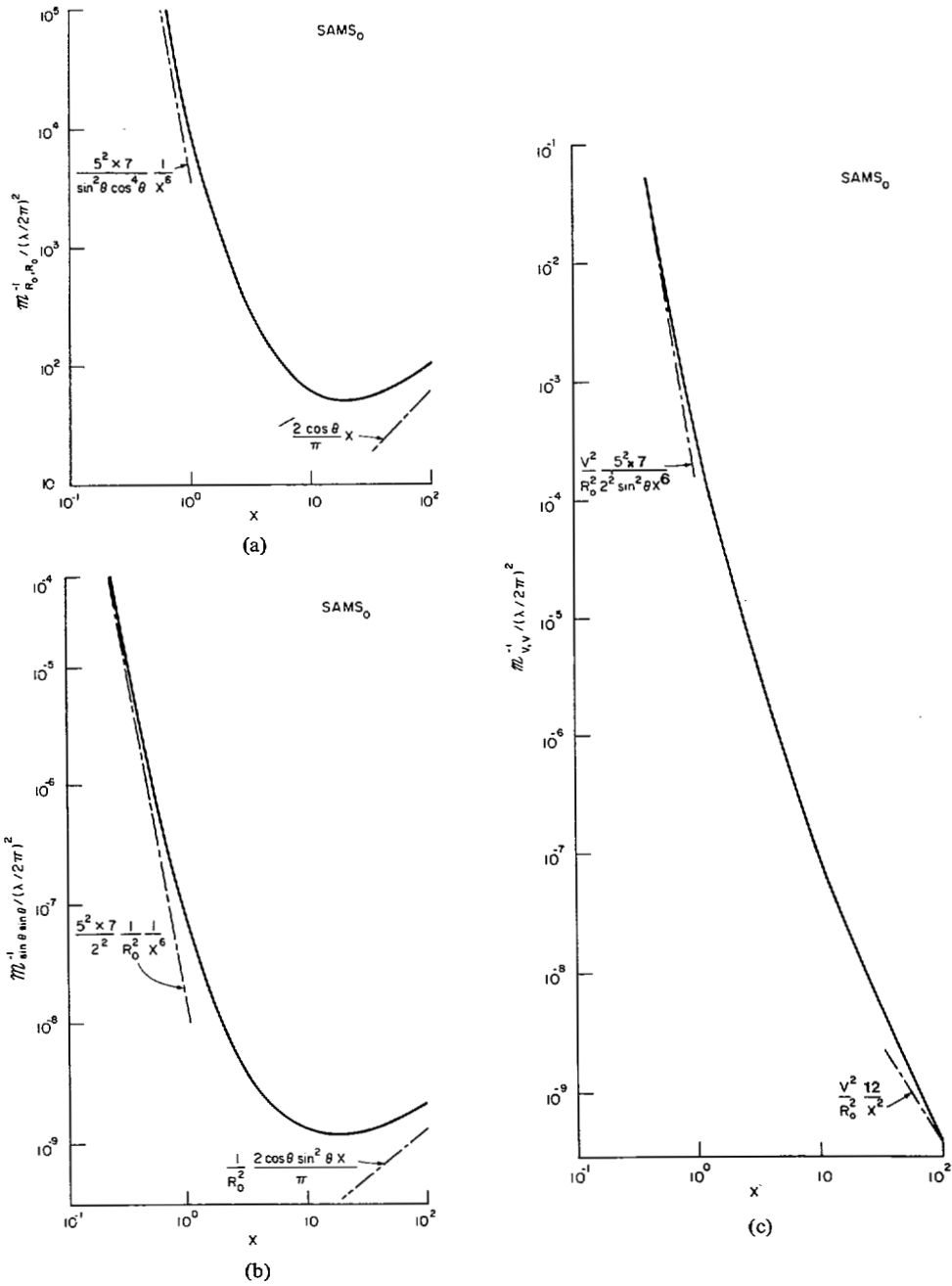
Fig. 10. · (a) Range mean-square spread versus X. (b) Angle mean-square spread versus X. (c) Speed mean-square spread versus X.

$[R_0 v]^T$, and the local expressions are

$$M_{R_0,v}^{-1} \cong \left(\frac{\lambda}{2\pi}\right)^2$$

$$\cdot \begin{bmatrix} \dfrac{45}{\cos^4\theta X^4} & \vdots & -\dfrac{v}{R_0}\dfrac{3(11\sin^2\theta - 2)}{\sin^2\theta \cos^2\theta X^2} \\ \cdots\cdots\cdots & \vdots & \cdots\cdots\cdots \\ = & \vdots & \dfrac{v^2}{R_0{}^2}\dfrac{3}{\sin^2\theta X^2} \end{bmatrix} \quad (26a)$$

$$\det M_{R_0,v} \cong \left(\frac{2\pi}{\lambda}\right)^6 \frac{R_0{}^2}{v^2} \frac{\sin^2\theta \cos^4\theta}{135} X^6. \quad (26b)$$

The degree of coupling is specified by the cross correlation

$$\rho_{R_0,v} \cong -\frac{(11\sin^2\theta - 2)X}{\sqrt{15}\sin\theta}. \quad (26c)$$

The results for this problem parallel those for the range/angle estimation of Part I [9] upon rescaling the involved quantities. As happened there, the range is focused from the chirp (second-order) effects, while the source velocity is measured from the
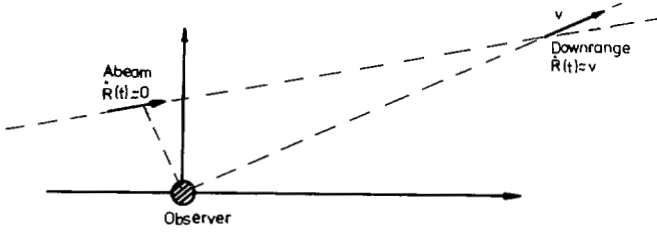
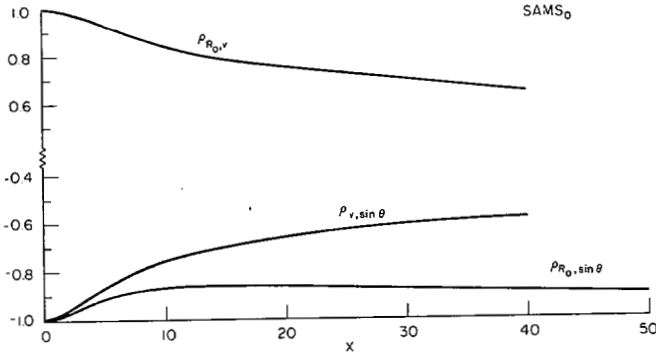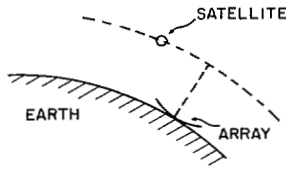Fig. 11. Source/observer geometry developing from abeam to down-range.

Fig. 12. Cross correlation versus X.

Fig. 13. Satellite tracking geometry.

linear modulations on the signal structure. The velocity spread increases monotonically as the geometry approaches broadside. This is intuitively clear: for broadside geometries the linear effects are minimum, and the velocity has to be measured from zero Doppler effects.

B. Velocity/Angle Estimates

Here the range is known by means, for example, of active measurement. The analysis brings up one of the major difficulties underlining the SAMS$_o$ estimation problem: the high correlation between the error on the velocity and angle estimates. The parameter vector is $A = [v \sin \theta]^T$ and the local expressions

$$M_{v, \sin \theta}^{-1} \cong \left(\frac{\lambda}{2\pi}\right)^2$$
$$\cdot \begin{bmatrix} \dfrac{v^2}{R_0^2} \dfrac{45}{4X^4} & \vdots & -\dfrac{v}{R_0^2} \dfrac{45 \sin \theta}{4X^4} \\ \cdots & \cdots & \cdots \\ & \vdots & \dfrac{1}{R_0^2} \dfrac{45 \sin^2 \theta}{4X^4} \end{bmatrix} \quad (27a)$$

$$\det M_{v, \sin \theta} \cong \left(\frac{2\pi}{\lambda}\right)^4 \frac{R_0^4}{v^2} \frac{4X^6}{135}. \quad (27b)$$

Note that the velocity and the angle mean-square spreads, given by the diagonal elements of M^{-1}, depend on the 4th order of X^{-1}, as compared with the previous application (or with the problem in Part I [9]), where they were a function of X^{-2}. The main lobe is oriented along the down-range velocity component $v_s = v \sin \theta$. The cross correlation between the parameter errors is $\rho_{v, \sin \theta} \approx -1 + \alpha(\theta)X^2$, which underlines the strong coupling between the errors on the velocity and angle estimates.

VI. ERROR PERFORMANCE ANALYSIS

The mean-square error performance of the two-step ML algorithm is discussed. The total mean-square error of the component A_j of the parameter vector A is decomposed into two terms. The first, referred to as the global mean-square error $\sigma_{gl_j}^2$, results from decision errors ϵ, or diversions, on the first step. The second, the local mean-square error $\sigma_{loc_j}^2$, depends on the flatness of the main lobe. For a detailed discussion of these errors in a similar context, see Part I [9], or [11].

A. Global Errors

Section IV established the peaked structure of the GAF. To pursue the error performance analysis of the ML receiver, the GAF is reduced to its ellipsoidal main lobe, being considered zero outside it. This justifies that the first step of the ML algorithm be modeled as an M-ary hypotheses decision problem with orthogonal signals over a Rayleigh channel. To determine the total number M of hypotheses, the grid has to be dimensioned. The main lobe ellipsoid is taken as the elementary cell. Its volume is, apart from a constant, measured by $\det M$. Then

$$M = \frac{V_\Omega}{k} (\det M)^{1/2} \quad (28)$$

where k is a normalizing constant and V_Ω is the volume of the a priori region of interest in the parameter space.

For large energy signal-to-noise ratio (SNR) and large number M of grid cells, the probability of error $\Pr(\epsilon)$ and the conditional mean-square error for the M-ary hypotheses decision problem considered can be easily determined (see [9]–[11, pp. 302–307], [15]) leading to

$$\sigma_{gl_j}^2 \approx \frac{\Delta_M A_j^2}{6} \Pr(\epsilon) \quad (29a)$$

with

$$\Pr(\epsilon) \cong \left(\ln M - \frac{1}{2M} + \gamma\right) \Big/ (E_r/N_0) \quad (29b)$$

where γ is the Euler constant and $\Delta_M A_j$ is the a priori uncertainty of parameter $A_j, j = 1, 2, 3$.

B. Local Errors

The main lobe of the GAF has been conveniently described in Section V by the ellipsoid (21c). This second-order descrip-

tion of the GAF justifies [11] that the local mean-square error be estimated from the Cramer-Rao bounds. For this type of problem (see [9] or [11]), the Cramer-Rao inequality is

$$\Lambda_\epsilon \triangleq E[(A_{ml} - A_a)(A_{ml} - A_a)^*] \geqslant J^{-1} \qquad (30a)$$

where the Fisher information matrix

$$J = GM \qquad (30b)$$

with

$$G = 2\frac{\bar{E}_r}{N_0}\frac{\bar{E}_r}{N_0 + \bar{E}_r}. \qquad (30c)$$

Expressions (29) and (30) stress once again the importance of M. Substituting the expressions given in Section V, one obtains analytical formula for the errors (see [12]). Here, graphical studies are pursued.

Fig. 14 shows as a function of X the total mean-square error

$$\sigma_{tot_j}^2 = E(A_{j_\epsilon}^2) = E(A_j - A_{j_{ml}})^2 = a_{gl_j}^2 + \sigma_{loc_j}^2 \qquad (31)$$

as well as its global and local components for the following two a priori regions of interest:

$$\Omega = \begin{cases} \Delta_M R_0 = R_{0_M} - R_{0_m} = 6 \times 10^5 \text{ ft} \\ \Delta_M v = v_M - v_m = 3 \text{ ft/s} \\ \Delta_M \theta = \theta_M - \theta_m = 5° \end{cases}$$

$$\Omega' = \Omega_2 = \begin{cases} \Delta_M R_0 = 6 \times 10^5 \text{ ft} \\ \Delta_M v = 1.5 \text{ ft/s} \\ \Delta_M \theta = 1°. \end{cases} \qquad (32)$$

The source is located at the values given by (19) and the remaining parameters assumed are

SNR = 0 dB

$\lambda = 50$ ft $L = 250$ ft $\sigma_b^2 = 0.5$.

For small X, the local component dominates (Pr (ϵ) is very small). After a transition region where both components are of the same order, it is the global errors that dominate the performance. Observe that, for the conditions assumed, the transitional region takes place first for the range parameter, at values of X bounded to occur in many applications of practical interest.

The effect of reducing the a priori region of interest is twofold (see (29a)): a change in Pr (ϵ), purely reflected in Fig. 14 (c), and a change in the a priori uncertainty of the parameters.

For $X < 1$, Fig. 15 shows the dependence of the Cramer-Rao bounds on the actual source angle θ. The value of SNR = -3 dB. The range standard deviation σ_{R_0} displays a convex cup behavior, with a maximum range performance occurring at $\theta \approx 35°$, value that can be predicted [12] by the local analysis. This performance deteriorates monotonically as the geometry approaches either "broadside" (large errors in the velocity
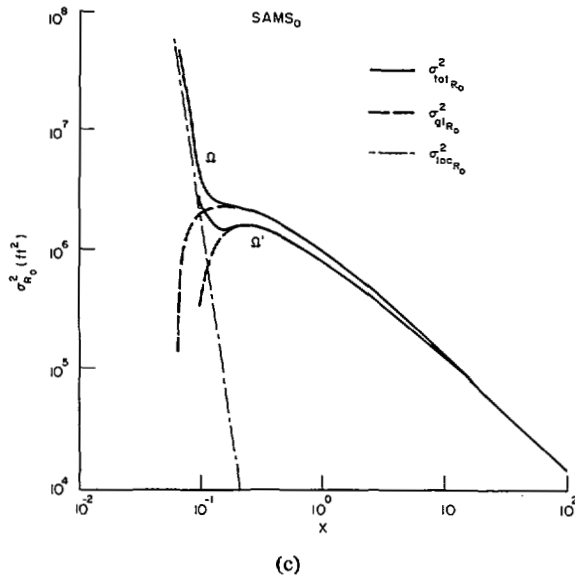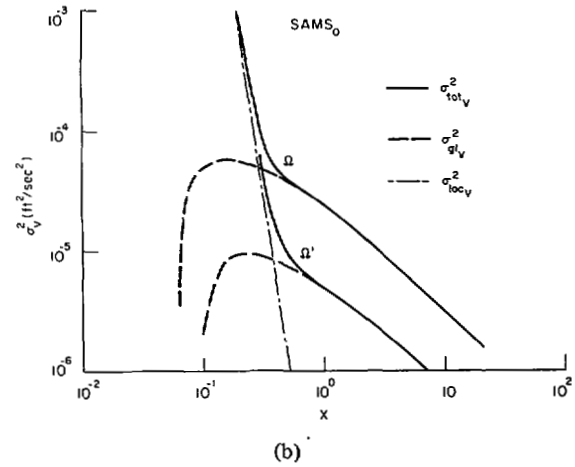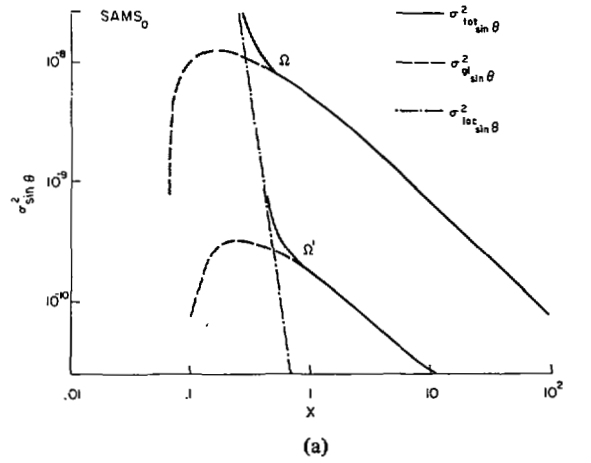

(a)

(b)

(c)

Fig. 14.   (a) Speed total ML performance versus X.   (b) Angle total ML performance versus X.   (c) Range total ML performance versus X.

parameter) or "end-fire" (reduction of effective array length) conditions. With respect to the speed performance, one concludes as already noted that σ_v increases sharply at "broadside" (vanishing down-range velocity), decreasing monotoni-
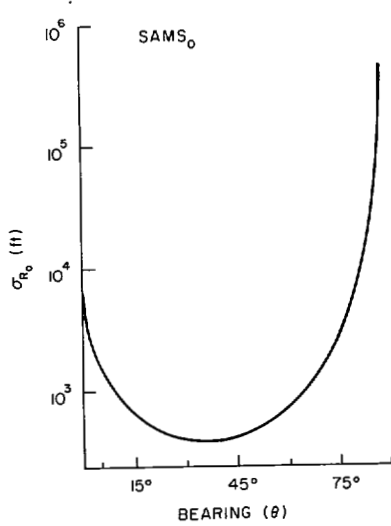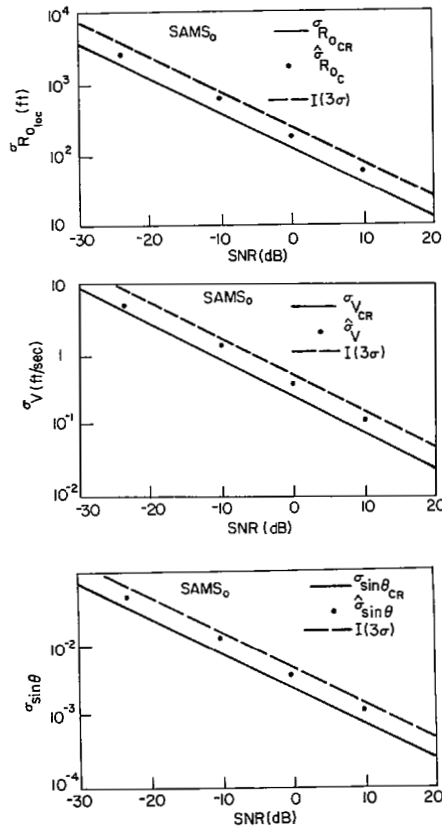
Fig. 15.   Range Cramer–Rao bound versus bearing.

Fig. 16.   SAMSo simulation results.

The curves show that all statistically computed standard deviations are within the 3σ-confidence interval $I(3\sigma)$ of the theoretically evaluated Cramer–Rao standard deviation.

VII. CONCLUSION

The paper considered the tracking by an omnidirectional passive observer of a point moving source radiating narrow-band signals. Assuming deterministic dynamics, the relative geometry was parameterized, the simple model developed fitting a three-parameter nonlinear estimation framework. The ML receiver was designed and its structure and associated errors were analyzed with emphasis laid on the passive global range observability as obtained from the higher order phase modulations induced on the signal structure by the temporal problem diversity. Global and local mean-square error bounds were presented, with graphical displays exploring the effects of the geometry on the mean-square error performance. Considering short and long observation intervals, approximate expressions were derived, having been shown how they compare with the exact bounds.

Depending solely on the geometry, the two-step practical implementation of the ML receiver exhibited two distinct performance behaviors: on a local geometry, the mean-square performance is well approximated by the local bounds determined by the sharpness and dimensions of the ambiguity structure main lobe; on a global geometry the performance is given by the global bounds measuring the large inaccuracies induced on the average by the decision errors occurring on the crude search. The analysis was tested via Monte Carlo simulation studies, the experimental results being within the 3σ-confidence interval of the theoretical ones. The theory and expressions presented here can be applied, as in [12], to dimension receivers that passively acquire the global geometry in navigation and positioning applications. Part III [10] generalizes the passive $SAMS_0$ model to include directional arrays tracking moving sources.

ACKNOWLEDGMENT

cally when the geometry approaches "end-fire" (Doppler configuration).

Fig. 16 compares, for different SNR values, the statistical behavior of the ML algorithm, as predicted by the foregoing analysis and as obtained by Monte Carlo simulation. The assumed parameters are

$$\lambda = 50 \text{ ft} \qquad \sigma_b{}^2 = 1 \qquad L = 50 \text{ ft} \qquad X = 0.287$$

$$R_0 = 6 \times 10^3 \text{ ft} \qquad \theta = -15° \qquad v = 30 \text{ ft/s}.$$

REFERENCES

[1]   A. W. Rihaczek, *Principles of High-Resolution Radar.* New York: McGraw-Hill, 1969.
[2]   R. O. Harger, *Synthetic Aperture Radar Systems Theory and Design.* New York: Academic Press, 1970.
[3]   A. E. E. Rogers, "Very long baseline-interferometry with large effective bandwidth for phase-delay measurements," *Radio Sci.,* vol. 5, pp. 1239–1248, 1970.
[4]   E. B. Fomalont, "Earth rotation aperture synthesis," *Proc. IEEE,* vol. 61, pp. 1211–1218, Sept. 1973.
[5]   T. Hagfors and D. B. Campbell, "Mapping of planetary surfaces by radar," *Proc. IEEE,* vol. 61, pp. 1219–1225, Sept. 1973.
[6]   R. C. Spindel and R. P. Porter, "Precision tracking systems for sonobuoys," in *Proc. IEEE Int. Conf. on Engineering in the Ocean Environment, Ocean 74,* vol. II.
[7]   *IEEE Trans. Geosci. Electron. (Special Issue on Data Collection*

from Multiple Earth Platforms), vol. GE-13, Jan. 1975.

[8] C. P. Wang, "Laser anemometry," *Amer. Sci.,* vol. 5, no. 3, pp. 289–298, May–June 1977.

[9] J. M. F. Moura and A. B. Baggeroer, "Passive systems theory with narrow-band and linear constraints: Part I–Spatial diversity," *IEEE J. Oceanic Eng.,* vol. OE-3, Jan. 1978.

[10] J. M. F. Moura, "Passive systems theory with narrow-band and linear constraints: Part III–Spatial/temporal diversity," to be published.

[11] H. L. Van Trees, *Detection, Estimation and Modulation Theory. Part III.* New York: Wiley, 1971.

[12] J. M. F. Moura, "Passive systems theory with applications to positioning and navigation," Res. Lab. of Electr., Massachusetts Inst. Technol., Cambridge, Rep. No. 490, Apr. 1976.

[13] L. S. Cahoon and M. J. Hinich, "A method for locating targets using range only," *IEEE Trans. Inform. Theory,* vol. IT-22, pp. 217–225, Mar. 1976.

[14] E. E. Westerfield, "Determination of position of a drifting buoy by means of the Navy navigation satellite system," in *Proc. IEEE Conf. Eng. Ocean Environment,* pp. 443–446, 1972.

[15] P. M. Woodward, *Probability and Information Theory, with Applications to Radar.* New York: McGraw-Hill, 1955.

[16] H. L. Van Trees, *Detection, Estimation, and Modulation Theory: Part I.* New York: Wiley, 1968.

[17] M. Abramowitz and I. A. Stegun, *Handbook of Mathematical Functions.* New York: Dover, 1965.

[18] A. Papoulis, *Systems and Transforms with Applications in Optics.* New York: McGraw-Hill, 1967.